

# An improved weighted essentially non-oscillatory scheme for hyperbolic conservation laws

Rafael Borges<sup>a</sup>, Monique Carmona<sup>a</sup>, Bruno Costa<sup>a,\*</sup>, Wai Sun Don<sup>b</sup>

<sup>a</sup> *Departamento de Matemática Aplicada, IM-UFRJ, Caixa Postal 68530, Rio de Janeiro, RJ, CEP 21945-970, Brazil*

<sup>b</sup> *Division of Applied Mathematics, Brown University, Providence, Rhode Island 02912, United States*

Received 22 September 2007; received in revised form 15 November 2007; accepted 21 November 2007

Available online 8 December 2007

## Abstract

In this article we develop an improved version of the classical fifth-order weighted essentially non-oscillatory finite difference scheme of [G.S. Jiang, C.W. Shu, Efficient implementation of weighted ENO schemes, *J. Comput. Phys.* 126 (1996) 202–228] (WENO-JS) for hyperbolic conservation laws. Through the novel use of a linear combination of the low order smoothness indicators already present in the framework of WENO-JS, a new smoothness indicator of higher order is devised and new non-oscillatory weights are built, providing a new WENO scheme (WENO-Z) with less dissipation and higher resolution than the classical WENO. This new scheme generates solutions that are sharp as the ones of the mapped WENO scheme (WENO-M) of Henrick et al. [A.K. Henrick, T.D. Aslam, J.M. Powers, Mapped weighted essentially non-oscillatory schemes: achieving optimal order near critical points, *J. Comput. Phys.* 207 (2005) 542–567], however with a 25% reduction in CPU costs, since no mapping is necessary. We also provide a detailed analysis of the convergence of the WENO-Z scheme at critical points of smooth solutions and show that the solution enhancements of WENO-Z and WENO-M at problems with shocks comes from their ability to assign substantially larger weights to discontinuous stencils than the WENO-JS scheme, not from their superior order of convergence at critical points. Numerical solutions of the linear advection of discontinuous functions and nonlinear hyperbolic conservation laws as the one dimensional Euler equations with Riemann initial value problems, the Mach 3 shock–density wave interaction and the blastwave problems are compared with the ones generated by the WENO-JS and WENO-M schemes. The good performance of the WENO-Z scheme is also demonstrated in the simulation of two dimensional problems as the shock–vortex interaction and a Mach 4.46 Richtmyer–Meshkov Instability (RMI) modeled via the two dimensional Euler equations.

© 2007 Elsevier Inc. All rights reserved.

MSC: 65P30; 77Axx

**Keywords:** Weighted essentially non-oscillatory; Hyperbolic conservation laws; Smoothness indicators; WENO weights

\* Corresponding author. Tel.: +55 2562 7402.

E-mail addresses: [rborges@ufrj.br](mailto:rborges@ufrj.br) (R. Borges), [carmona@ufrj.br](mailto:carmona@ufrj.br) (M. Carmona), [bcosta@ufrj.br](mailto:bcosta@ufrj.br) (B. Costa), [wsdon@dam.brown.edu](mailto:wsdon@dam.brown.edu) (W.S. Don).

## 1. Introduction

In the numerical simulation of compressible flows modeled by means of hyperbolic conservation laws in the form

$$\frac{\partial \mathbf{u}}{\partial t} + \nabla \cdot \mathbf{F}(\mathbf{u}) = 0, \quad (1)$$

the development of finite time discontinuities generates  $O(1)$  oscillations, known as the Gibbs phenomenon, causing loss of accuracy and numerical instability. Among many choices of shock capturing schemes such as the piecewise parabolic method (PPM) [7], the essentially non-oscillatory scheme (ENO) [6], high-order weighted essentially non-oscillatory schemes (WENO) [1,2] have been extensively used for the simulation of the fine scale and delicate structures of the physical phenomena related to shock–turbulence interactions.

WENO schemes owe their success to the use of a dynamic set of stencils, where a nonlinear convex combination of lower order polynomials adapts either to a higher order approximation at smooth parts of the solution, or to an upwind spatial discretization that avoids interpolation across discontinuities and provides the necessary dissipation for shock capturing. The nonlinear coefficients of the convex combination, hereafter referred to as weights, are based on the local smoothness indicators, which measure the sum of the normalized squares of the scaled  $L^2$  norms of all derivatives of the lower order polynomials [2]. An essentially zero weight is assigned to those lower order polynomials whose underlining stencils contain high gradients and/or shocks, yielding an essentially non-oscillatory solution at discontinuities. At smooth parts of the solution, higher order is achieved through the mimicking of the central upwinding scheme of maximum order, when all smoothness indicators are about the same size. Hence, an efficient design of these smoothness indicators is a very important issue for WENO schemes.

The classical choice of smoothness indicators in [2] generated weights that failed to recover the maximum order of the scheme at points of the solution where the first or higher derivatives of the flux function vanish. This fact was clearly pointed out at Henrick et al. [3]. In their study, necessary and sufficient conditions on the weights, for optimality of the order, were derived and a correcting mapping to be applied to the classical weights was devised. The resulting mapped WENO scheme of [3] recovered the optimal order of convergence at critical points of a smooth function and presented sharper results close to discontinuities. In this article, we follow a different approach, which is to improve on the classical smoothness indicators to obtain weights that satisfies the sufficient conditions for optimal order. Taylor series analysis of the classical smoothness indicators reveals that a simple combination of them would give higher order information about the regularity of the numerical solution. The incorporation of this new higher order information into the weights definition improves the convergence order at the critical points of smooth parts of the solution, as well as decreases the dissipation close to discontinuities, while maintaining stability and the essentially non-oscillatory behavior.

The enhancements of the new scheme come from the larger weights that it assigns to discontinuous stencils. Contrary to common belief, the strategy should be to augment the influence of the stencil containing the discontinuity as much as possible, without destroying the essentially non-oscillatory behavior. A comparison of the weights of the classical, the mapped and the new WENO scheme close to a discontinuity shows that the ratio between the weight of a discontinuous stencil and a continuous one increases slightly from the classical weights to the mapped weights, and increases substantially with the new weights proposed in this article. The computational cost of the new scheme is the same as the WENO-JS and around 75% of WENO-M.

This paper is organized as follows: in Section 2, the classical WENO scheme of Jiang and Shu [2] and the mapped weights version of Henrick et al. [3] are described and some of the relevant analytical results are reviewed. The new WENO scheme is introduced in Section 3 where a detailed discussion about the new smoothness indicator is given. In Section 4, we analyze the order of convergence of WENO-Z at critical points of a smooth solution. In Section 5, all three schemes are compared with the numerical simulation of the linear advection of discontinuous functions, the one dimensional Euler equations with Riemann initial values problems (SOD, LAX and 123), the Mach 3 shock density–wave interaction and the interactive blastwaves problems. We end the article showing results on the two dimensional Mach 3 shock–vortex interaction and the Mach 4.46 Richtmyer–Meshkov Instability (RMI) along with the CPU timing of the three WENO schemes. Concluding remarks are given in Section 6.

## 2. Weighted essentially non-oscillatory schemes

In this section, we briefly describe the fifth-order weighted essentially non-oscillatory conservative finite difference scheme when applied to hyperbolic conservation laws as in (1). Without loss of generality, we will restrict our discussion to the one dimensional scalar case. Extensions to system of equations and higher spatial dimensions present no extra complexity with regards to our main point which is the design of new weights for the WENO scheme.

Consider an uniform grid defined by the points  $x_i = i\Delta x$ ,  $i = 0, \dots, N$ , which are also called cell centers, with cell boundaries given by  $x_{i\pm\frac{1}{2}} = x_i \pm \frac{\Delta x}{2}$ , where  $\Delta x$  is the uniform grid spacing. The semi-discretized form of (1), by the method of lines, yields a system of ordinary differential equations

$$\frac{du_i(t)}{dt} = -\left.\frac{\partial f}{\partial x}\right|_{x=x_i}, \quad i = 0, \dots, N, \quad (2)$$

where  $u_i(t)$  is a numerical approximation to the point value  $u(x_i, t)$ . A conservative finite difference formulation for hyperbolic conservation laws requires high-order consistent numerical fluxes at the cell boundaries in order to form the flux differences across the uniformly spaced cells. The conservative property of the spatial discretization is obtained by implicitly defining the numerical flux function  $h(x)$  as

$$f(x) = \frac{1}{\Delta x} \int_{x-\frac{\Delta x}{2}}^{x+\frac{\Delta x}{2}} h(\xi) d\xi,$$

such that the spatial derivative in (2) is exactly approximated by a conservative finite difference formula at the cell boundaries,

$$\frac{du_i(t)}{dt} = \frac{1}{\Delta x} (h_{i+\frac{1}{2}} - h_{i-\frac{1}{2}}), \quad (3)$$

where  $h_{i\pm\frac{1}{2}} = h(x_{i\pm\frac{1}{2}})$ .

High-order polynomial interpolations to  $h_{i\pm\frac{1}{2}}$  are computed using known grid values of  $f$ ,  $f_i = f(x_i)$ . The classical fifth-order WENO scheme uses a 5-points stencil, hereafter named  $S^5$ , which is subdivided into three 3-points stencils  $\{S_0, S_1, S_2\}$ , as shown in Fig. 1. The fifth-order polynomial approximation  $\hat{f}_{i\pm\frac{1}{2}} = h_{i\pm\frac{1}{2}} + O(\Delta x^5)$  is built through the convex combination of the interpolated values  $\hat{f}^k(x_{i\pm\frac{1}{2}})$ , in which  $f^k(x)$  is the third degree polynomial below, defined in each one of the stencils  $S_k$ :

$$\hat{f}_{i\pm\frac{1}{2}} = \sum_{k=0}^2 \omega_k \hat{f}^k(x_{i\pm\frac{1}{2}}), \quad (4)$$

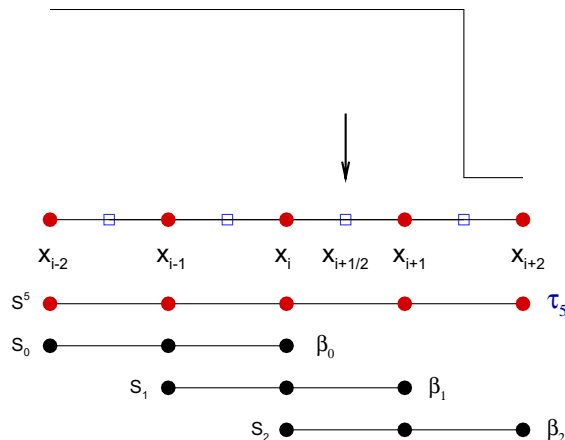


Fig. 1. The computational uniform grid  $x_i$  and the 5-points stencil  $S^5$ , composed of three 3-points stencils  $S_0, S_1, S_2$ , used for the fifth-order WENO reconstruction step.

where

$$\hat{f}^k(x_{i+\frac{1}{2}}) = \hat{f}_{i+\frac{1}{2}}^k = \sum_{j=0}^2 c_{kj} f_{i-k+j}, \quad i = 0, \dots, N. \quad (5)$$

The  $c_{kj}$  are Lagrangian interpolation coefficients (see [2]), which depend on the left-shift parameter  $k = 0, 1, 2$ , but not on the values  $f_i$ .

It can be shown by Taylor series expansion of (5) that

$$\hat{f}_{i+\frac{1}{2}}^k = h_{i+\frac{1}{2}} + A_k \Delta x^3 + O(\Delta x^4), \quad (6)$$

where the values  $A_k$  are independent of  $\Delta x$ .

The weights  $\omega_k$  are defined as

$$\omega_k = \frac{\alpha_k}{\sum_{l=0}^2 \alpha_l}, \quad \alpha_k = \frac{d_k}{(\beta_k + \epsilon)^p}. \quad (7)$$

The coefficients  $d_0 = \frac{3}{10}$ ,  $d_1 = \frac{3}{5}$ ,  $d_2 = \frac{1}{10}$  are called the ideal weights since they generate the central upstream fifth-order scheme for the 5-points stencil  $S^5$ . We refer to  $\alpha_k$  as the unnormalized weights. The parameter  $\epsilon$  is used to avoid the division by zero in the denominator and  $p = 2$  is chosen to increase the difference of scales of distinct weights at non-smooth parts of the solution.

The smoothness indicators  $\beta_k$  measure the regularity of the  $k$ th polynomial approximation  $\hat{f}^k(x_i)$  at the stencil  $S_k$  and are given by

$$\beta_k = \sum_{l=1}^2 \Delta x^{2l-1} \int_{x_{i-\frac{1}{2}}}^{x_{i+\frac{1}{2}}} \left( \frac{d^l}{dx^l} \hat{f}^k(x) \right)^2 dx. \quad (8)$$

The expression of the  $\beta_k$  in terms of the cell averaged values of  $f(x)$ ,  $f_i$  are given by

$$\beta_0 = \frac{13}{12} (f_{i-2} - 2f_{i-1} + f_i)^2 + \frac{1}{4} (f_{i-2} - 4f_{i-1} + 3f_i)^2, \quad (9)$$

$$\beta_1 = \frac{13}{12} (f_{i-1} - 2f_i + f_{i+1})^2 + \frac{1}{4} (f_{i-1} - f_{i+1})^2, \quad (10)$$

$$\beta_2 = \frac{13}{12} (f_i - 2f_{i+1} + f_{i+2})^2 + \frac{1}{4} (3f_i - 4f_{i+1} + f_{i+2})^2. \quad (11)$$

and their Taylor series expansions at  $x_i$  are

$$\beta_0 = f_i'^2 \Delta x^2 + \left( \frac{13}{12} f_i''^2 - \frac{2}{3} f_i' f_i''' \right) \Delta x^4 - \left( \frac{13}{6} f_i'' f_i''' - \frac{1}{2} f_i' f_i^{(4)} \right) \Delta x^5 + O(\Delta x^6), \quad (12)$$

$$\beta_1 = f_i'^2 \Delta x^2 + \left( \frac{13}{12} f_i''^2 + \frac{1}{3} f_i' f_i''' \right) \Delta x^4 + O(\Delta x^6), \quad (13)$$

$$\beta_2 = f_i'^2 \Delta x^2 + \left( \frac{13}{12} f_i''^2 - \frac{2}{3} f_i' f_i''' \right) \Delta x^4 + \left( \frac{13}{6} f_i'' f_i''' - \frac{1}{2} f_i' f_i^{(4)} \right) \Delta x^5 + O(\Delta x^6). \quad (14)$$

The general idea of the weights definition (7) is that on smooth parts of the solution, the smoothness indicators  $\beta_k$  are all small and about the same size, generating weights  $\omega_k$  that are good approximations to the ideal weights  $d_k$ . On the other hand, if the stencil  $S_k$  contains a discontinuity,  $\beta_k$  is  $O(1)$  and the corresponding weight  $\omega_k$  is small relatively to the other weights. This implies that the influence of the polynomial approximation of  $h_{i+\frac{1}{2}}$  taken across the discontinuity is diminished up to the point where the convex combination (4) is essentially non-oscillatory. Fig. 1 shows the case where stencil  $S_2$  is discontinuous, yielding  $\beta_0$  and  $\beta_1$  to be much smaller than  $\beta_2$ . By (7), this results on  $\omega_2$  being a small number in the convex combination (4) (see also Fig. 3(a) of Section 3).

The process synthesized by (4) and (5) is called the WENO reconstruction step, for it reconstructs the values of  $h(x)$  at the cell boundaries of the interval  $I_i = [x_{i-\frac{1}{2}}, x_{i+\frac{1}{2}}]$  from its cell averaged values  $f(x)$  in the stencils

$\{S_k, k = 0, 1, 2\}$ . In [3], truncation error analysis of the finite difference Eq. (3) led to necessary and sufficient conditions on the weights  $\omega_k$  for the WENO scheme to achieve the formal fifth-order ( $O(\Delta x^5)$ ) convergence at smooth parts of the solution. It was also found that at first-order critical points  $x_c$ , points where the first derivative of the solution vanishes ( $f'(x_c) = 0$ ), convergence degraded to only third-order ( $O(\Delta x^3)$ ), a fact that was hidden by the homogenization of the weights caused by the use of a relatively large value for  $\epsilon$  in (7). Since this analysis is relevant to the description of the new WENO scheme introduced at next section, we recall its essential steps.

Adding and subtracting  $\sum_{k=0}^2 d_k \hat{f}_{i \pm \frac{1}{2}}^k$  to (4), gives:

$$\hat{f}_{i \pm \frac{1}{2}} = \sum_{k=0}^2 d_k \hat{f}_{i \pm \frac{1}{2}}^k + \sum_{k=0}^2 (\omega_k^\pm - d_k) \hat{f}_{i \pm \frac{1}{2}}^k = \left[ h_{i \pm \frac{1}{2}} + B^\pm \Delta x^5 + O(\Delta x^6) \right] + \sum_{k=0}^2 (\omega_k^\pm - d_k) \hat{f}_{i \pm \frac{1}{2}}^k. \quad (15)$$

(The superscripts  $\pm$  corresponds to the  $\pm$  in the  $f_{i \pm \frac{1}{2}}^k$ .) Expanding the second term with the help of (6) we obtain:

$$\sum_{k=0}^2 (\omega_k^\pm - d_k) \hat{f}_{i \pm \frac{1}{2}}^k = \sum_{k=0}^2 (\omega_k^\pm - d_k) \left( h_{i \pm \frac{1}{2}} + A_k \Delta x^3 + O(\Delta x^4) \right) \quad (16)$$

$$= h_{i \pm \frac{1}{2}} \sum_{k=0}^2 (\omega_k^\pm - d_k) + \Delta x^3 \sum_{k=0}^2 A_k (\omega_k^\pm - d_k) + \sum_{k=0}^2 (\omega_k^\pm - d_k) O(\Delta x^4). \quad (17)$$

Substituting the result above at a finite difference formula for the polynomial approximation  $\hat{f}_{i \pm \frac{1}{2}}$ :

$$\frac{\hat{f}_{i+\frac{1}{2}} - \hat{f}_{i-\frac{1}{2}}}{\Delta x} = \frac{h_{i+\frac{1}{2}} - h_{i-\frac{1}{2}}}{\Delta x} + O(\Delta x^5) + \frac{\sum_{k=0}^2 (\omega_k^+ - d_k) \hat{f}_{i+\frac{1}{2}}^k - \sum_{k=0}^2 (\omega_k^- - d_k) \hat{f}_{i-\frac{1}{2}}^k}{\Delta x} \quad (18)$$

$$= f'(x_i) + O(\Delta x^5) + \left[ \frac{h_{i+\frac{1}{2}} \sum_{k=0}^2 (\omega_k^+ - d_k) - h_{i-\frac{1}{2}} \sum_{k=0}^2 (\omega_k^- - d_k)}{\Delta x} \right] \\ + \Delta x^2 \sum_{k=0}^2 A_k (\omega_k^+ - \omega_k^-) + \left[ \sum_{k=0}^2 (\omega_k^+ - d_k) - \sum_{k=0}^2 (\omega_k^- - d_k) \right] O(\Delta x^3). \quad (19)$$

The  $O(\Delta x^5)$  term remains after division by  $\Delta x$  because  $B^+ = B^-$  in (15). Thus, necessary and sufficient conditions for fifth-order convergence in (3) are given by

$$\sum_{k=0}^2 (\omega_k^\pm - d_k) = O(\Delta x^6), \quad (20)$$

$$\sum_{k=0}^2 A_k (\omega_k^+ - \omega_k^-) = O(\Delta x^3), \quad (21)$$

$$\omega_k^\pm - d_k = O(\Delta x^2). \quad (22)$$

Note that due to normalization  $\sum_{k=0}^2 \omega_k^\pm = \sum_{k=0}^2 d_k$ , so the first constraint is always satisfied and, from (17), we see that a sufficient condition for fifth-order of convergence is simply given by

$$\omega_k^\pm - d_k = O(\Delta x^3). \quad (23)$$

Let us now check how the classical WENO weights  $\omega_k$  (7) behave with respect to the restrictions above. It was shown in [3] that if the smoothness indicators  $\beta_k$  satisfy  $\beta_k = D(1 + O(\Delta x^p))$ , then the weights  $\omega_k$  satisfy  $\omega_k = d_k + O(\Delta x^p)$ , where  $D$  is a non-zero constant independent of  $k$ . Looking at the Taylor series expansions of the smoothness indicators  $\beta_k$  in (12)–(14), we see that  $\beta_k = D(1 + O(\Delta x^2))$ , implying that  $\omega_k = d_k + O(\Delta x^2)$ . This requires that condition (21) must be as well satisfied in order for the classical WENO to have the expected fifth-order convergence. This indeed happens and can be easily confirmed with any symbolic calculation.

Nevertheless, at critical points this situation becomes more complex depending on the number of vanishing derivatives of  $f$ . For instance, if only the first derivative vanishes, then  $\beta_k = D(1 + O(\Delta x))$  and  $\omega_k = d_k + O(\Delta x)$ , degrading the convergence of the scheme to third order only. If the second derivative also vanishes, then convergence decreases even more to second order.

A fix to this deficiency of the classical weights  $\omega_k$  was proposed in [3] through the application of a mapping function that increased the approximation of  $\omega_k$  to the ideal weights  $d_k$  at critical points to the required third-order  $O(\Delta x^3)$  in (23). The mapping function  $g_k(\omega)$  used in [3] is defined as

$$g_k(\omega) = \frac{\omega(d_k + d_k^2 - 3d_k\omega + \omega^2)}{d_k^2 + \omega(1 - 2d_k)} \quad (24)$$

and is a non-decreasing monotone function with the following properties:

1.  $0 \leq g_k(\omega) \leq 1$ ,  $g_k(0) = 0$  and  $g_k(1) = 1$ .
2.  $g_k(\omega) \approx 0$  if  $\omega \approx 0$ ;  $g_k(\omega) \approx 1$  if  $\omega \approx 1$ .
3.  $g_k(d_k) = d_k$ ,  $g'_k(d_k) = g''_k(d_k) = 0$ .
4.  $g_k(\omega) = d_k + O(\Delta x^6)$ , if  $\omega = d_k + O(\Delta x^2)$ .

Numerical results in [3] confirmed the usefulness of the mapping, since with the modified weights the resulting WENO scheme (WENO-M) recovered the full fifth-order convergence at critical points of a smooth solution. Note, however, that if at a critical point the second derivative also vanishes, then  $\beta_k = D(1 + O(1))$ , implying  $\omega_k = d_k + O(1)$  (see Eqs. (12)–(14)) and the mapping is unable to improve the weights approximation, maintaining the same second order of convergence as the classical WENO.

**Remark 1.** For problems with shocks, the  $O(1)$  truncation error at the discontinuities diminishes the advantages of such order improvements at critical points. Nevertheless, the numerical results obtained by the mapped scheme of [3] are clearly superior to the ones of the classical WENO even for problems with shocks at the initial conditions. Distinctly from [3], we do not credit these enhancements of the numerical solution to the higher order of approximation of the mapped weights at critical points, but to the smaller dissipation that results from the assignment of larger weights to discontinuous stencils when using the mapped scheme. As we shall see in the next section, the new WENO scheme assign weights to stencils with discontinuities that are even larger than the mapped WENO ones, generating even sharper solutions, while still maintaining the non-oscillatory property.

### 3. The new WENO scheme

In this section, we devise a new set of WENO weights  $\omega_k$  that satisfies the necessary and sufficient conditions (22) for fifth-order convergence. The novel idea is to use the whole 5-points stencil  $S^5$  (see Fig. 1) to devise a new smoothness indicator of higher order than the classical smoothness indicators  $\beta_k$ . We denote it by  $\tau_5$  and it is simply defined as the absolute difference between  $\beta_0$  and  $\beta_2$  at  $x_i$ , namely

$$\tau_5 = |\beta_0 - \beta_2|. \quad (25)$$

It is straightforward to see from (12)–(14) that the truncation error of  $\tau_5$  is

$$\frac{13}{3} |f''_i f'''_i| \Delta x^5 + O(\Delta x^6) \quad (26)$$

and that it is a measure of the higher derivatives of  $f$ , when they exist, and is indeed computed using the whole 5-points stencil  $S^5$ . Here, we list the important properties of  $\tau_5$ :

- If  $S^5$  does not contain discontinuities, then  $\tau_5 = O(\Delta x^5) \ll \beta_k$  for  $k = 0, 1, 2$ ;
- if the solution is continuous at some of the  $S_k$ , but discontinuous in the whole  $S^5$ , then  $\beta_k \ll \tau_5$ , for those  $k$  where the solution is continuous;
- $\tau_5 \leq \max_k \beta_k$ .

We now define the new smoothness indicators  $\beta_z^k$  as

$$\beta_z^k = \left( \frac{\beta_k + \epsilon}{\beta_k + \tau_5 + \epsilon} \right), \quad k = 0, 1, 2 \quad (27)$$

and the new WENO weights  $\omega_k^z$  as

$$\omega_k^z = \frac{\alpha_k^z}{\sum_{l=0}^2 \alpha_l^z}, \quad \alpha_k^z = \frac{d_k}{\beta_k^z} = d_k \left( 1 + \frac{\tau_5}{\beta_k + \epsilon} \right), \quad k = 0, 1, 2, \quad (28)$$

where  $\epsilon$  is a small number (see the remark below) used to avoid the division by zero in the denominator of (27). All  $\beta_k^z$  are smaller than unity and they are all close to 1 at smooth parts of the solution. They are in fact the normalization of the classical smoothness indicators  $\beta_k$  by the higher order information contained in  $\tau_5$ .

The following notation will be used in order to distinguish between the three different WENO schemes considered in this work. The mapped weights of [3] are denoted as  $\omega_k^M$  and the resulting mapped WENO scheme as WENO-M. The new WENO scheme, introduced below, is referred as WENO-Z and the superscript  $z$  is added to all quantities related to it. To keep a coherent notation throughout the article, the classical WENO weights and smoothness indicators carry no superscript, although, the classical WENO scheme of [2] is referred as WENO-JS.

**Remark 2.** The role of the parameter  $\epsilon$  was discussed in [3], where it was shown that the value of  $1 \times 10^{-6}$ , commonly suggested in the literature, would dominate over the smoothness indicators  $\beta_k$  at the denominators of the classical WENO weights, hiding the suboptimal performance of the classical scheme on critical points. In this work, we use much smaller values of  $\epsilon$  for the WENO-M and WENO-Z schemes, that will be clearly indicated along with the numerical experiments, in order to force this parameter to play only its original role of not allowing vanishing denominators at the weights definitions.

We now investigate the order of approximation of the new weights  $\omega_k^z$  with respect to the ideal weights  $d_k$ . We first study the case where there are no critical points. These will be studied separately in the next section. We also take  $\epsilon = 0$  in the analysis below. It is straightforward to check from (12)–(14) and the properties of  $\tau_5$  that, at smooth parts of the solution,

$$\left( 1 + \frac{\tau_5}{\beta_k} \right) = 1 + O(\Delta x^3), \quad k = 0, 1, 2$$

and from (28),

$$\omega_k^z = d_k + O(\Delta x^3), \quad k = 0, 1, 2. \quad (29)$$

Thus, the new weights  $\omega_k^z$  satisfy the sufficient condition (23), providing the formal fifth order of accuracy to the WENO-Z scheme at non-critical points of a smooth solution.

Let us take a look at a numerical example through the discontinuous function:

$$u(x, 0) = f(x) = \begin{cases} -\sin(\pi x) - \frac{1}{2}x^3 & -1 < x < 0, \\ -\sin(\pi x) - \frac{1}{2}x^3 + 1 & 0 \leq x \leq 1, \end{cases} \quad (30)$$

consisting of a piecewise sine function with a jump discontinuity at  $x = 0$ .

Fig. 2(a) shows the numerical solutions of the wave equation  $u_t = u_x$  at  $t = 8$ , for the WENO-JS, WENO-M and WENO-Z schemes, with (30) as initial condition, along with the exact solution. Fig. 2(b) shows the values of the smoothness indicators  $\beta_0, \beta_1, \beta_2$  and of the high-order smoothness indicator  $\tau_5$  of the WENO-Z scheme with  $\epsilon = 10^{-40}$ . Note that  $\tau_5$  is only comparable to one of the  $\beta_k$  at stencils that include the discontinuity.

Next, we examine the new weights  $\omega_k^z$  on stencils containing discontinuities and confirm their distinction with respect to the classical weights. Consider the simple case of a shock localized in stencil  $S_2$ , while the solution in stencils  $S_0$  and  $S_1$  are smooth (see Fig. 1). The ratios between  $\beta_0, \beta_1$  and  $\beta_2$  are larger than the same ratios using the classical weights:

$$\frac{\beta_k^z}{\beta_2^z} = \frac{\beta_k}{\beta_2} \frac{\beta_2 + \tau_5}{\beta_k + \tau_5} \geq \frac{\beta_k}{\beta_2}, \quad k = 0, 1, \quad (31)$$

where we used the fact that  $\beta_2 > \beta_k$ ,  $k = 0, 1$ .

This has the straightforward implication that the relative importance of the stencil  $S_2$ , the one containing the discontinuity, is increased in the final convex combination of the WENO-Z scheme (see Fig. 3(a)–(c)).



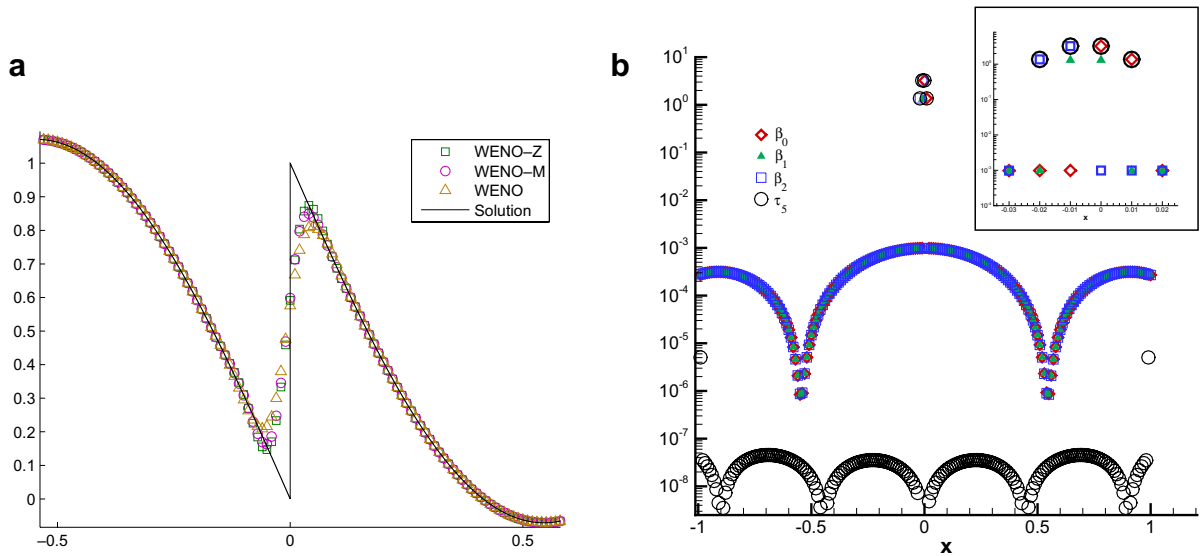


Fig. 2. (a) Numerical solutions of the linear wave equation with the discontinuous initial condition (30) at  $t = 8$  for the WENO-JS, WENO-M and WENO-Z schemes. The exact solution is shown in a solid line. (b) The values of the smoothness indicators  $\beta_0, \beta_1, \beta_2$  and of the high-order smoothness indicator  $\tau_5$  of the WENO-Z scheme with  $\epsilon = 10^{-40}$ .

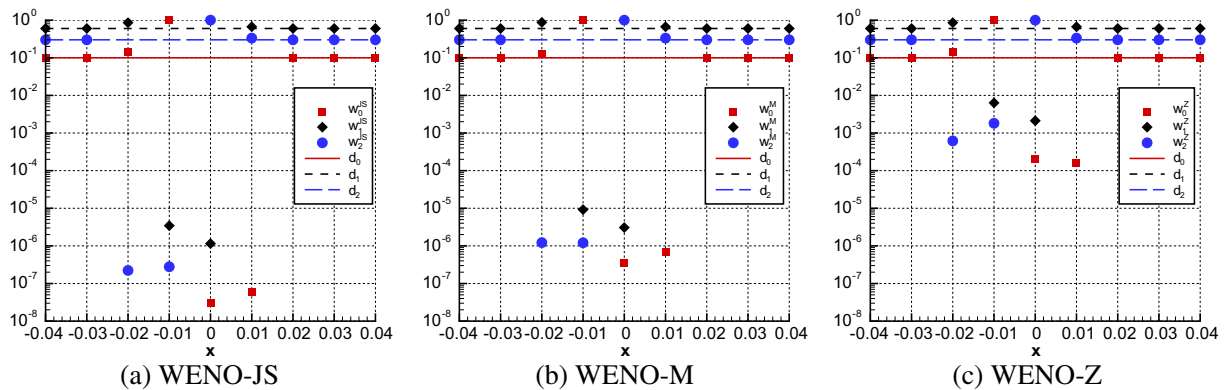


Fig. 3. The distribution of the ideal weights  $d_k$  and the weights  $\omega_k, k = 0, 1, 2$  for (a) WENO-JS ( $\epsilon = 10^{-6}$ ), (b) WENO-M ( $\epsilon = 10^{-40}$ ) and (c) WENO-Z ( $\epsilon = 10^{-40}$ ) schemes at the first step of the numerical solution of the wave equation  $u_t = u_x$ , with periodic initial condition given by (30). The ideal weights  $d_k$  are shown in lines and the weights  $\omega_k$  are shown in symbols. The vertical axis is shown in  $\log_{10}$  scale.

Fig. 3(a)–(c) show the weights  $\omega_k$ , for the WENO-JS ( $\epsilon = 10^{-6}$ ), WENO-M ( $\epsilon = 10^{-40}$ ) and WENO-Z ( $\epsilon = 10^{-40}$ ) schemes at the first step of the numerical solution of the wave equation  $u_t = u_x$ , with periodic initial condition given by (30). The ideal weights  $d_k$  are also plotted as lines and the vertical axis is in  $\log_{10}$  scale.

- Far away from the discontinuity  $x = 0$ , the weights  $\omega_k$  (symbols) for all schemes correctly match the corresponding ideal weights  $d_k$  (lines).
- $x = -0.02$  is the first location where the 5-points stencil  $S^5$  contains the discontinuity. At this grid point, the rightmost stencil  $S_2$  has its weight  $\omega_2$  decreased to a much smaller value than  $\omega_0$  and  $\omega_1$ , while these two are slightly increased to reflect their larger relevance at the reconstruction step.
- At  $x = -0.01$ , the discontinuity is present at  $S_1$  and  $S_2$  and a small value is assigned to  $\omega_1$  as well, yielding  $\omega_0 \approx O(1)$ .
- At  $x = 0.01$ , a symmetric scenario occurs and  $\omega_2$  assumes the largest value.



While this situation is general for all schemes, the main difference is at the ratios between the weights for discontinuous and continuous stencils, as discussed above. While WENO-JS sets very small values for the discontinuous stencils, around  $10^{-8}$ , and the mapping of WENO-M generates a small increase on these values, WENO-Z yields a more substantial increase to  $10^{-4}$ . In different words, the convex combinations of WENO-M and WENO-Z are closer to the central scheme than the one of WENO-JS, incurring in less dissipation. Looking closer at the numerical solutions of Fig. 2(a), we also see that the approximation of WENO-Z is slightly sharper at the discontinuity.

**Remark 3.** In the numerical experiments of Section 5 we will once again notice this slightly superior sharpness of WENO-Z with respect to WENO-M at problems with discontinuities. Nevertheless, as we should also see in Section 5, it is on their computational costs that they differ more, since WENO-Z takes about 25% less CPU time than WENO-M.

The larger values of weights for the discontinuous stencils is one of the main differences of WENO-M and WENO-Z over the classical WENO-JS. Another one is their superior order of convergence at critical points of smooth solutions. This is the subject of next section.

#### 4. Convergence at critical points

In [3], it was detected that the classical fifth-order WENO scheme achieves only third order at critical points of smooth solutions. It was also demonstrated that this deficiency was being hidden by the large value of  $10^{-6}$  assigned to the parameter  $\epsilon$  in the definition of the weights. The mapping of the weights proposed in [3] recovered the formal fifth order at critical points and the enhanced numerical results in problems with shocks were credited to this fix. In this section we analytically demonstrate that WENO-Z is fourth-order accurate at critical points of a smooth solution and also present a further modification of the WENO-Z weights that recovers the fifth order of convergence at the critical points. Nevertheless, we also show that this modification increases the dissipation of the WENO-Z scheme.

We depart from formula (19) and notice that the order of the WENO scheme is given by

$$s = \min(5, s_1 + 2, s_2 + 3), \quad (32)$$

where

$$\sum_{k=0}^2 A_k (\omega_k^+ - \omega_k^-) = O(\Delta x^{s_1}), \quad (33)$$

$$\omega_k^\pm - d_k = O(\Delta x^{s_2}). \quad (34)$$

We will examine the values of  $s_1$  and  $s_2$  for a smooth function with a critical point of order  $n_{cp} \geq 1$ , which is a function  $f$  with vanishing derivatives for all order less than and equal to  $n_{cp}$ :

$$f'(x_c) = \dots = f^{(n_{cp})}(x_c) = 0, \quad (35)$$

where the superscript denotes the order of differentiation. To simplify notation, we drop the superscript  $Z$  for the WENO-Z weights  $\omega_k^Z$  in this section.

Using the definition of the WENO-Z weights (28), it is easily seen that

$$\alpha_k - d_k = d_k \frac{\tau_5}{\beta_k + \epsilon} \quad \text{implies} \quad \omega_k - d_k = O\left(\frac{\tau_5}{\beta_k + \epsilon}\right). \quad (36)$$

It is also easily seen from the Taylor series formulae (12)–(14) and (26) for the smoothness indicators  $\beta_k$  and  $\tau_5$  that in the presence of a critical point of order  $n_{cp}$ , we have

$$\beta_k = O(\Delta x^{2(n_{cp}+1)}) \quad \text{and} \quad \tau_5 = \begin{cases} O(\Delta x^5) & \text{if } n_{cp} \leq 1, \\ O(\Delta x^{2(n_{cp}+1)}) & \text{else.} \end{cases} \quad (37)$$

Applying these to (36), we obtain the value of  $s_2$  as below:

$$\omega_k - d_k = \begin{cases} O(\Delta x^3) & \text{if } n_{cp} = 0 \\ O(\Delta x) & \text{if } n_{cp} = 1 \\ O(1) & \text{if } n_{cp} \geq 2 \end{cases} \quad \text{or} \quad s_2 = \begin{cases} 3 & \text{if } n_{cp} = 0, \\ 1 & \text{if } n_{cp} = 1, \\ 0 & \text{if } n_{cp} \geq 2. \end{cases} \quad (38)$$

For  $s_1$ , we expand (33) as

$$\sum_{k=0}^2 A_k (\omega_k^+ - \omega_k^-) = \Omega^+ - \Omega^- = \frac{N^+ D^- - N^- D^+}{D^+ D^-}, \quad (39)$$

where

$$\Omega^\pm = \sum_{k=0}^2 A_k \omega_k^\pm = \frac{\sum_{k=0}^2 F_k^\pm(A_k)}{1 + \sum_{k=0}^2 F_k^\pm(1)} \quad \text{with } F_k^\pm(\gamma) = \tau_5^\pm \gamma \frac{d_k}{\beta_k}, \quad (40)$$

and

$$N^\pm = \tau_5^\pm \left( \prod_{k=0}^2 \beta_k^\pm \right) \sum_{k=0}^2 \frac{A_k d_k}{\beta_k^\pm}, \quad D^\pm = \left( \prod_{k=0}^2 \beta_k^\pm \right) + \tau_5^\pm \left( \prod_{k=0}^2 \beta_k^\pm \right) \sum_{k=0}^2 \frac{d_k}{\beta_k^\pm}, \quad (41)$$

where we used that  $\sum_{k=0}^2 A_k d_k = 0$  and  $\sum_{k=0}^2 d_k = 1$ .

The leading order of (39),  $s_1$ , can be found with the aid of a symbolic algebra program by substituting the Taylor series expansion of the smoothness indicators  $\beta_k$ , subjected to a critical point of order  $n_{cp}$  (see Table 1). The order of the WENO-Z scheme,  $s = \min(5, s_1 + 2, s_2 + 3)$ , is shown at Table 2. Note that WENO-Z attains order 4 at a first-order critical point, improving over WENO-JS which attains only order 3, as shown in [3]. See also Table 3 that shows the  $L^\infty$  error and rate of convergence of the WENO-JS and WENO-Z schemes for  $f(x) = x^3 + \cos(x)$ , which has a first-order critical point at  $x = 0$ , but whose third-order derivative is not zero. The computations were done in Matlab using its variable precision functions with 64 digits and a value of  $\epsilon = 10^{-40}$ . This was necessary because of the roundoff error in the standard double precision due to the very small values of  $\Delta x$  that had to be used in order to detect the fourth-order convergence of WENO-Z at the critical point.

Only a small modification on the formulae of the weights (28) is necessary to recover the fifth-order accuracy at a first-order critical point. If instead we define the new weights as

$$\omega_k^z = \frac{\alpha_k^z}{\sum_{l=0}^2 \alpha_l^z}, \quad \alpha_k^z = \frac{d_k}{\beta_k^z} = d_k \left( 1 + \left( \frac{\tau_5}{\beta_k + \epsilon} \right)^q \right), \quad k = 0, 1, 2, \quad (42)$$

with  $q = 2$ , then fifth order is achieved when  $n_{cp} = 1$ . Note that both definitions agree when  $q = 1$ . This is easy to understand, since for a smooth function, increasing the value of  $q$  in (42) decreases the correction of the WENO-Z weights to the ideal weights  $\{d_k\}$ , making the scheme closer to the optimal central scheme. On the other hand, for discontinuous problems, the ratio  $\frac{\tau_5}{\beta_k}$  is much larger for the continuous substencils than for the one containing the discontinuity. Therefore, increasing  $q$  decreases the relative importance of the discontinuous sub stencil, making the scheme more dissipative. Nevertheless, the results in Fig. 2, along with the ones of next section, show that due to the essential  $O(1)$  error of problems with discontinuities, fourth order of convergence at critical points does not keep WENO-Z, as simply defined in (28), with  $q = 1$ , to obtain results in problems with shocks that are equivalent to the ones of the WENO-M scheme. This confirms that the larger

Table 1

The leading order term of (39),  $s_1$ , as a function of  $n_{cp}$

	$n_{cp}$			
	0	1	2	$\geq 2$
$N^+ D^- - N^- D^+$	$O(\Delta x^{18})$	$O(\Delta x^{26})$	$O(\Delta x^{36})$	$O(\Delta x^{12(n_{cp})})$
$D^+ D^-$	$O(\Delta x^{12})$	$O(\Delta x^{24})$	$O(\Delta x^{36})$	$O(\Delta x^{12(n_{cp})})$
$s_1$	6	2	0	0

Table 2  
Order of convergence of the WENO-Z scheme

	$n_{cp}$			
	0	1	2	$\geq 2$
$s_1$	6	2	0	0
$s_2$	3	1	0	0
$s = \min(5, s_1 + 2, s_2 + 3)$	5	4	2	2

Table 3

The  $L^\infty$  error and rate of convergence of the WENO-JS and WENO-Z schemes (for  $q = 1$  and  $q = 2$ ) at the first-order critical point  $x = 0$  of the function  $f(x) = x^3 + \cos(x)$  with  $\epsilon = 10^{-40}$

$\Delta x$	WENO-JS		WENO-Z, $q = 1$		WENO-Z, $q = 2$	
	Error	Order	Error	Order	Error	Order
1.00e−3	0.16e−10		9.87e−12		2.08e−13	
5.00e−4	2.09e−10	2.95	6.45e−13	3.93	7.45e−15	4.80
2.50e−4	2.66e−11	2.97	4.12e−14	3.96	2.48e−16	4.91
1.25e−4	3.35e−12	2.98	2.60e−15	3.98	7.98e−18	4.96
6.25e−5	4.20e−13	2.99	1.63e−16	3.99	2.53e−19	4.98

weights attributed to discontinuous stencils by WENO-M and WENO-Z, although by distinct approaches, is the essential improvement of these schemes with respect to WENO-JS.

## 5. Numerical experiments

In this section, we compare the numerical performance of WENO-Z with the classical WENO-JS and its version with mapping, WENO-M. In all the numerical experiments below, WENO-Z refers to the definition in (28) and (42) with  $q = 1$ . This is to make the point that the smaller dissipation of WENO-Z, as pointed out before in Sections 3 and 4, has much more influence than its rate of convergence at critical points when solving problems with shocks. For that matter, the solutions obtained with both versions of WENO-Z,  $q = 1$  and  $q = 2$ , show the same order of convergence at discontinuous solutions, not justifying a separate presentation. A more detailed analysis of the WENO-Z schemes for several values of  $q$ , including higher orders versions, is left for an upcoming article.

The numerical presentation of this section starts with the solution of a classical problem of advection of a function with discontinuities, followed by the solution of the one dimensional Euler system of equations with Riemann initial value problems such as the Sod, Lax and 123; the Mach 3 shock–density wave interaction, the interactive blastwaves problem and finishes with 2D simulations on the shock–vortex interaction and the Mach 4.46 Richtmyer–Meshkov Instability (RMI) problem with a single mode perturbation along a xenon and argon gases interface.

In the following experiments, the ODEs resulting from the semi-discretized PDEs are evolved in time by the third-order total variation diminishing Runge–Kutta scheme (RK-TVD) [2]:

$$\begin{aligned}
 \vec{U}^1 &= \vec{U}^n + \Delta t L(\vec{U}^n), \\
 \vec{U}^2 &= \frac{1}{4}(3\vec{U}^n + \vec{U}^1 + \Delta t L(\vec{U}^1)), \\
 \vec{U}^{n+1} &= \frac{1}{3}(\vec{U}^n + 2\vec{U}^2 + 2\Delta t L(\vec{U}^2)),
 \end{aligned} \tag{43}$$

where  $L$  is the spatial operator. The CFL number is set to be 0.4 for all WENO schemes and  $\Delta t$  is bounded by  $\Delta x^{\frac{5}{3}}$ .

The numerical experiments presented here were run on a AMD Opteron(tm) 250 processor with 3 GB of memory. In order to ensure fairness in the comparison of CPU timings, all three schemes shared the same sub-routine calls and were compiled with the same compilation options including optimization ones. The only

differences between the implementation of the three WENO schemes were on the subroutines for computing the different related WENO weights. In all the experiments to follow, we took  $\epsilon = 10^{-6}$  for WENO-JS and  $\epsilon = 10^{-40}$  for WENO-M and WENO-Z, in order to compare with the classical scheme at its best.

### 5.1. The linear advection problem

In this section, we apply WENO-Z to the linear transport of discontinuous functions in the case of an initial condition consisting of a Gaussian, a triangle, a square-wave and a semi-ellipse, given by

$$u(x, 0) = \begin{cases} \frac{1}{6} [G(x, \beta, z - \delta) + 4G(x, \beta, z) + G(x, \beta, z + \delta)], & x \in [-0.8, -0.6], \\ 1, & x \in [-0.4, -0.2], \\ 1 - |10(x - 0.1)|, & x \in [0, 0.2], \\ \frac{1}{6} [F(x, \alpha, a - \delta) + 4F(x, \alpha, a) + F(x, \alpha, a + \delta)], & x \in [0.4, 0.6], \\ 0, & \text{otherwise,} \end{cases} \quad (44)$$

$$G(x, \beta, z) = e^{-\beta(x-z)^2},$$

$$F(x, \alpha, a) = \sqrt{\max(1 - \alpha^2(x - a)^2, 0)},$$

where the constants are  $z = -0.7$ ,  $\delta = 0.005$ ,  $\beta = \frac{\log 2}{36\delta^2}$ ,  $a = 0.5$  and  $\alpha = 10$ . The advection equation  $u_t = u_x$  was solved until the final time  $t = 8$  on the interval  $[-1, 1]$  with periodic boundary conditions and the results of WENO-Z are compared against the ones of WENO-JS and WENO-M, all shown in Table 4.

Figs. 4 and 5 along with Table 4 show that WENO-Z behaves quantitatively and qualitatively equivalent to WENO-M with regards to the improvements over WENO-JS. Note that the lower order of WENO-Z at the critical points is less relevant than its smaller dissipation if one wants to obtain sharper representations of the discontinuities.

### 5.2. One dimensional Euler equations

In this section, we present numerical experiments with the one dimensional system of the Euler equations for gas dynamics in strong conservation form:

$$\mathbf{Q}_t + \mathbf{F}_x = 0, \quad (45)$$

where

$$\mathbf{Q} = (\rho, \rho u, E)^T, \quad \mathbf{F} = (\rho u, \rho u^2 + P, (E + P)u)^T, \quad (46)$$

the equation of state is given by

$$P = (\gamma - 1) \left( E - \frac{1}{2} \rho u^2 \right), \quad \gamma = 1.4 \quad (47)$$

and  $\rho, u, P$  and  $E$  are the density, velocity, pressure and total energy respectively.

Table 4

The  $L_1$  error and its rate of convergence for the WENO-JS, WENO-Z and WENO-M schemes, when solving the linear transport equation with the discontinuous initial condition (44) at the final time  $t = 8$

N	WENO-JS		WENO-Z		WENO-M	
	Error	Order	Error	Order	Error	Order
50	4.64e-1		3.14e-1		3.29e-1	
100	2.11e-1	1.13	1.65e-1	0.93	1.69e-1	0.91
200	9.32e-2	1.18	6.78e-2	1.28	7.04e-2	1.29
400	4.01e-2	1.21	3.10e-2	1.12	3.23e-2	1.12
800	1.94e-2	1.05	1.53e-2	1.01	1.59e-2	1.01
1600	9.93e-3	0.96	7.73e-3	0.99	8.06e-3	0.98

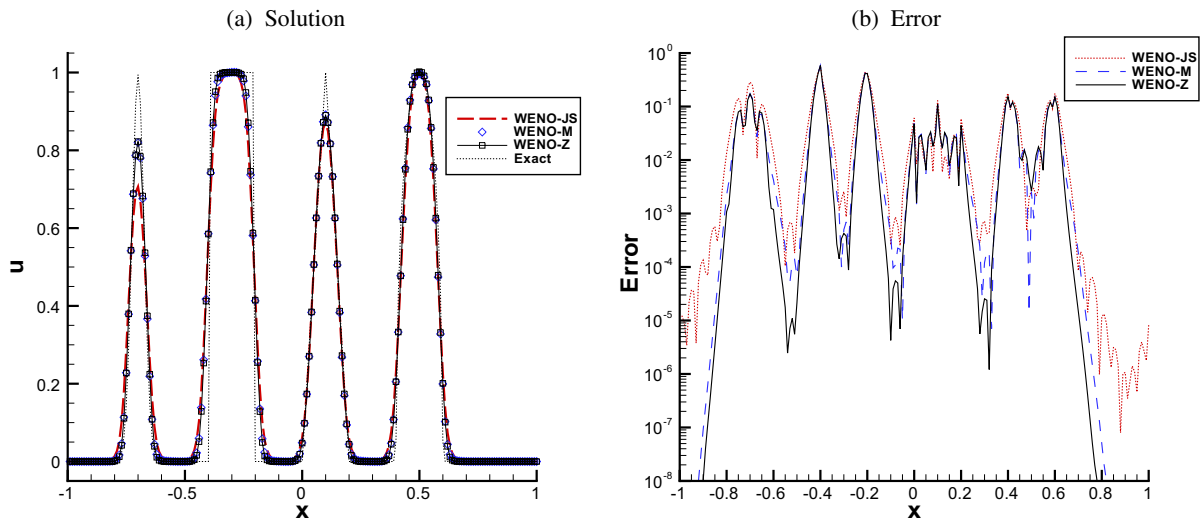


Fig. 4. Numerical solution and absolute pointwise error of the advection equation with the discontinuous initial condition (44) as computed by the WENO-JS, WENO-M and WENO-Z with  $N = 200$  at  $t = 8$ .

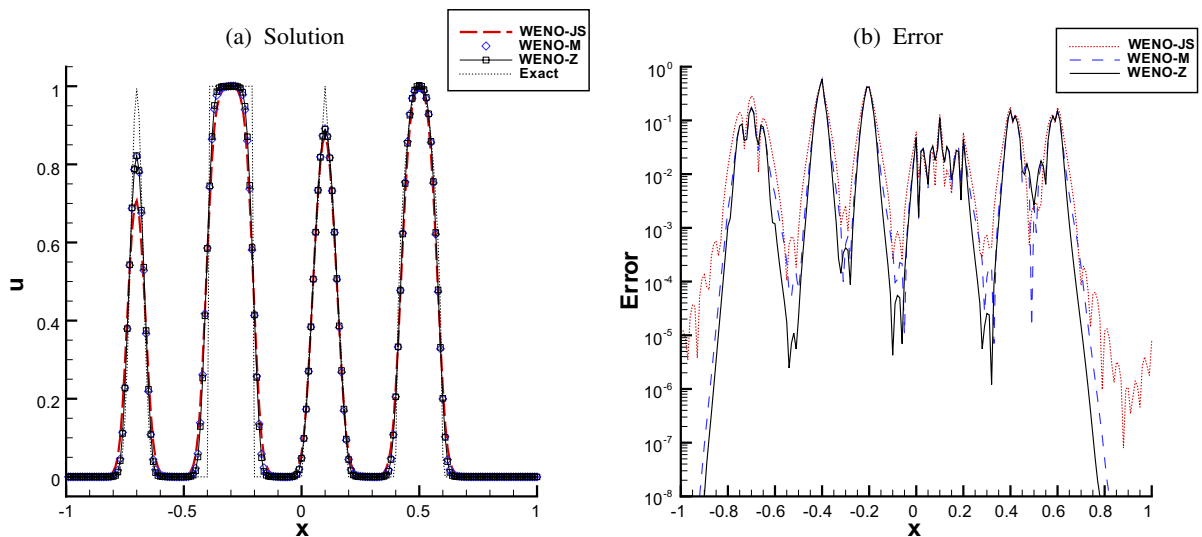


Fig. 5. Numerical solution and absolute pointwise error of the advection equation with the discontinuous initial condition (44) as computed by the WENO-JS, WENO-M and WENO-Z with  $N = 400$  at  $t = 8$ .

Following [1], the hyperbolicity of the Euler equations admits a complete set of right and left eigenvectors for the Jacobian of the system. The eigenvalues and eigenvectors are obtained via the linearized Riemann solver of Roe [4] and the first-order Lax-Friedrichs flux is used as the low order building block for the high-order reconstruction step of the WENO schemes (see Eq. (2.5) in [1]). After projecting the fluxes on the characteristic fields via the left eigenvectors, the high-order WENO reconstruction step is applied to obtain the high-order approximation at the cell boundaries, which are projected back into the physical space via the right eigenvectors. See [1] for further details of the algorithm.

### 5.2.1. Riemann initial value problems: Sod, Lax and 123

In this section, we show that the WENO-Z scheme passes the test of the Riemann initial value problems, also known as the shock-tube problems: the Sod problem, the Lax problem and the 123 problem. The numerical experiments were conducted using 200 grid points.

For the Sod problem, the density  $\rho$ , velocity  $U$  and pressure  $P$  in the left and the right stages of the shock are:

$$(\rho, U, P) = \begin{cases} (0.125, & 0, & 0.1) & -5 \leq x < 0, \\ (1, & 0, & 1) & 0 \leq x < 5 \end{cases} \quad (48)$$

and the final time is  $t = 2$ .

For the Lax problem, the density  $\rho$ , velocity  $U$  and pressure  $P$  in the left and the right stages of the shock are:

$$(\rho, U, P) = \begin{cases} (0.445, & 0.698, & 0.3528) & -5 \leq x < 0, \\ (0.500, & 0.000, & 0.5710) & 0 \leq x \leq 5 \end{cases} \quad (49)$$

and the final time is  $t = 1.3$ .

For the 123 problem, the density  $\rho$ , velocity  $U$  and pressure  $P$  in the left and the right stages of the shock are:

$$(\rho, U, P) = \begin{cases} (1, & -2, & 0.4) & -5 \leq x < 0, \\ (1, & 2, & 0.4) & 0 \leq x \leq 5 \end{cases} \quad (50)$$

and the final time is  $t = 1$ .

Numerical results from all schemes follow the same pattern as before, with WENO-Z and WENO-M being more accurate than the classical scheme due to their lesser dissipativity. The simulated density  $\rho$  of the Sod, Lax and 123 problems are shown in Fig. 6. The numerical results (symbols) are shown along with the exact solutions (solid black lines).

### 5.2.2. Shock–density wave interaction

In this section, we consider the one dimensional Mach 3 shock-entropy wave interaction [5], specified by the following initial conditions:

$$(\rho, u, P) = \begin{cases} (3.857143, & 2.629369, & \frac{31}{3}) & -5 \leq x < -4, \\ (1 + 0.2 \sin(kx), & 0, & 1) & -4 \leq x \leq 5, \end{cases} \quad (51)$$

where  $x \in [-5, 5]$  and  $k = 5$ . The solution of this problem consists of a number of shocklets and fine scale structures which are located behind a right-going main shock.

Fig. 7(a) and (b) provide a comparison for all schemes at  $t = 2$  with an increasing number of points. We shall refer to the solution computed by the WENO-M scheme with  $N = 2000$  points as the “exact” solution. At a low resolution,  $N = 200$ , as shown in Fig. 7(a), WENO-M and WENO-Z capture much more fine scale structures of the solution than WENO-JS, particularly at the high-frequency waves behind the shock.

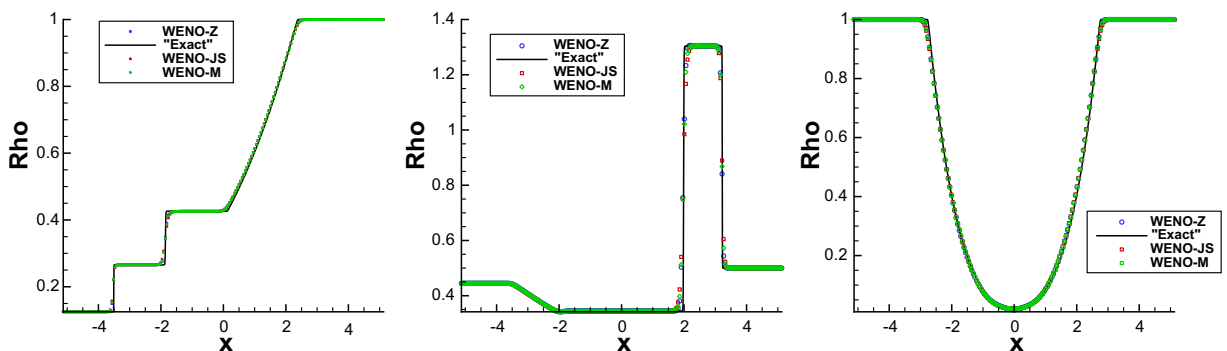


Fig. 6. The density profiles of the Sod, Lax and 123 problems with  $N = 200$  at times  $t = 2$ ,  $t = 1.3$  and  $t = 1$ , respectively. The solid black lines are the exact solutions.

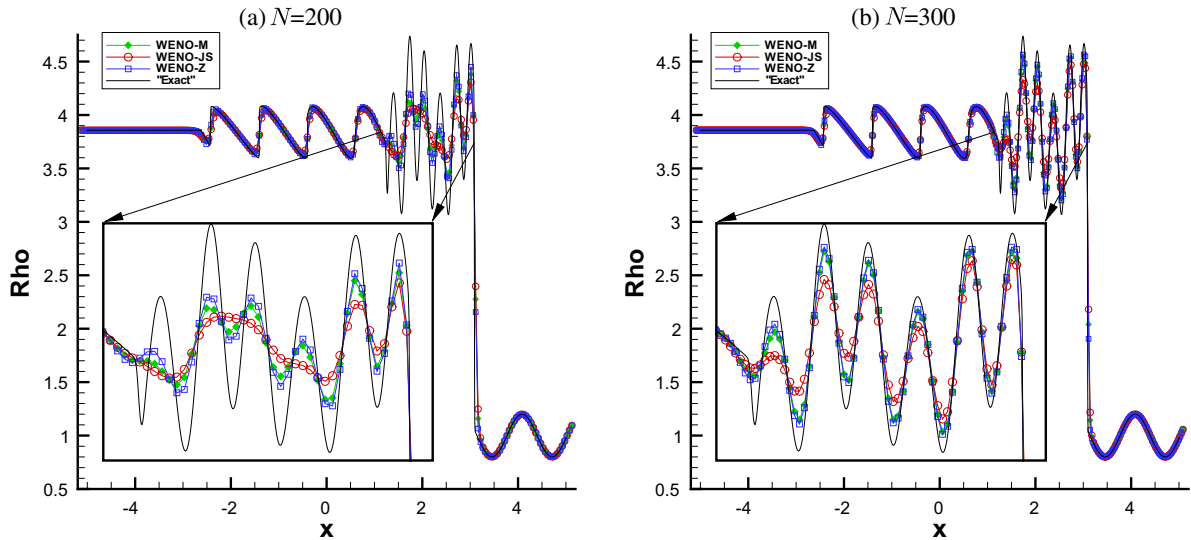


Fig. 7. Solution of the Mach 3 shock–density wave interaction with  $k = 5$  as computed by WENO-JS, WENO-M and WENO-Z schemes, at time  $t = 2$  with (a)  $N = 200$ , (b)  $N = 300$  points. The “exact” solution is computed by the WENO-M scheme with  $N = 2000$  points.

Increasing the resolution to  $N = 300$ , as shown in Fig. 7(b), we see that both WENO-M and WENO-Z converge faster than WENO-JS.

In Fig. 8, the wave number  $k$  is increased to 10, yielding rougher numerical approximations at the sine wave density field perturbation. As before, WENO-M and WENO-Z show much more accurate results than the classical WENO-JS.

### 5.2.3. Interacting blastwaves

The one dimensional blastwaves interaction problem of Woodward and Collela [7] has the following initial condition, with reflective boundary conditions:

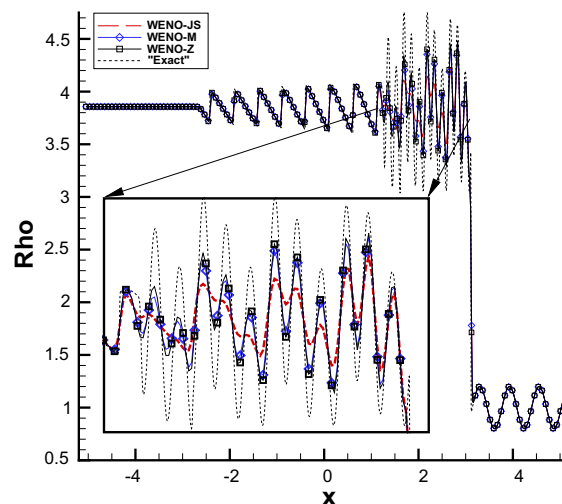


Fig. 8. Solution of the Mach 3 shock–density wave interaction with  $k = 10$  computed by the WENO-JS, WENO-M and WENO-Z with  $N = 510$  points. For clarity, only symbols at every fourth data point are plotted. The “exact” solution is computed by the WENO-M scheme with  $N = 2000$  points.



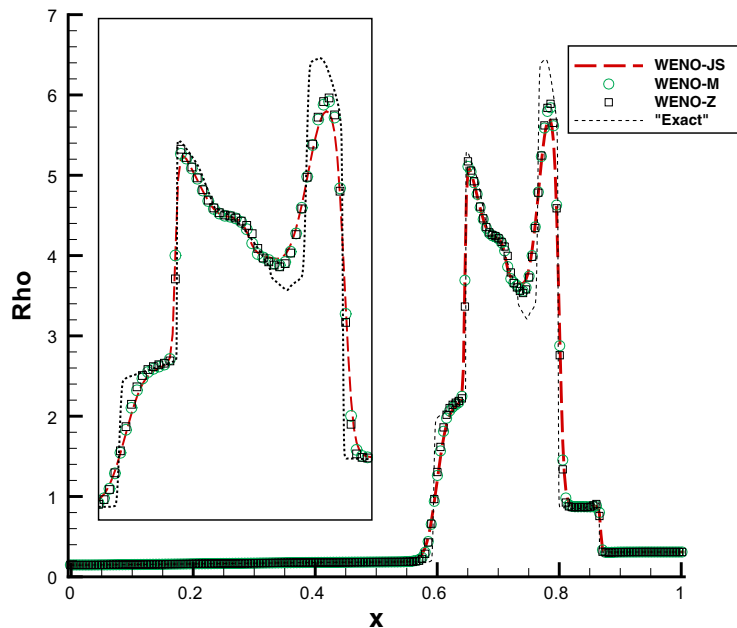


Fig. 9. Solution of the interactive blastwaves problem computed by the WENO-JS, WENO-M and WENO-Z with  $N = 400$  points. For clarity, only symbols at every other data point are plotted. The “exact” solution is computed by the WENO-M scheme with  $N = 4000$  points.

$$(\rho, U, P) = \begin{cases} (1, 0, 1000) & 0 \leq x < 0.1, \\ (1, 0, 0.01) & 0.1 \leq x < 0.9, \\ (1, 0, 100) & 0.9 \leq x \leq 1.0. \end{cases} \quad (52)$$

The initial pressure gradients generate two density shock waves that collide and interact later in time, forming a profile as shown in Fig. 9 at  $t = 0.038$ . All three schemes converge, as the number of points increase, to the reference solution computed by the WENO-M with  $N = 4000$  points. As before, WENO-M and WENO-Z show an improved convergence with respect to WENO-JS, due to their smaller dissipation. Fig. 10 presents a separate, and more detailed, comparison between WENO-M and WENO-Z, at two different portions of the domain. Careful examination of Fig. 10(a) shows that WENO-Z obtains a sharper peak near  $x = 0.78$ . In Fig. 10(b), the high-gradient structure at  $x = 0.86$  is better resolved with WENO-Z, as well as the contact discontinuity near  $x = 0.8$ .

### 5.3. Two dimensional Euler equations

In this section, we apply the WENO schemes to

- the Shock–vortex interaction (SV); and
- the Richtmyer–Meshkov instability (RMI)

in a rectangular domain.

The governing equations are the two-dimensional Euler equations in Cartesian coordinates given by

$$\mathbf{Q}_t + \mathbf{F}_x + \mathbf{G}_y = 0, \quad (53)$$

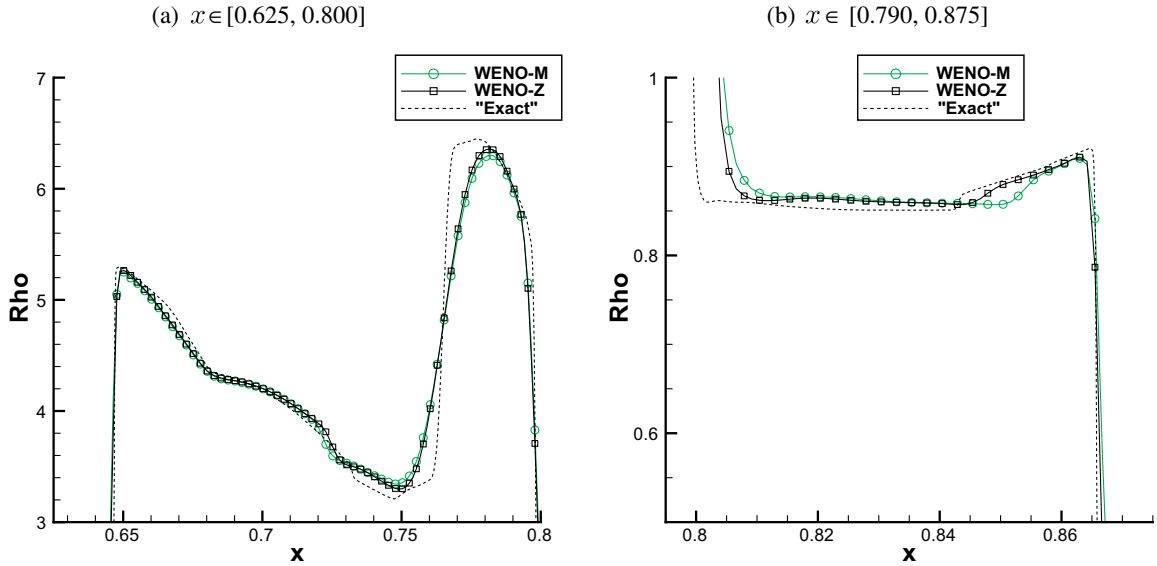


Fig. 10. Zoom in regions of the solution of the interactive blastwaves problem computed by the WENO-M and WENO-Z scheme with  $N = 800$  points. For clarity, only symbols at every other data point are plotted. The “exact” solution is computed by the WENO-M scheme with  $N = 4000$  points.

where

$$\begin{aligned} \mathbf{Q} &= (\rho, \rho u, \rho v, E)^T, \\ \mathbf{F} &= (\rho u, \rho u^2 + P, \rho uv, (E + P)u)^T, \\ \mathbf{G} &= (\rho v, \rho uv, \rho v^2 + P, (E + P)v)^T \end{aligned} \quad (54)$$

and the equation of state is

$$P = (\gamma - 1)(E - \frac{1}{2}\rho(u^2 + v^2)), \quad \gamma = 1.4. \quad (55)$$

Free stream inflow and outflow boundary conditions are imposed in the inflow and outflow boundaries, respectively, in the  $x$ -direction. A periodical boundary condition is imposed in the  $y$ -direction.

### 5.3.1. Shock–vortex interaction

The tangential velocity profile of the counter-clockwise rotating vortex [8] centered at  $(x_c, y_c)$  is given in polar coordinates by

$$U(r) = \begin{cases} \Gamma r(r_0^{-2} - r_1^{-2}), & 0 \leq r \leq r_0 < r_1, \\ \Gamma r(r^{-2} - r_1^{-2}), & r_0 \leq r \leq r_1, \\ 0, & r > r_1, \end{cases} \quad (56)$$

where  $r_0 = 0.2$ ,  $r_1 = 1.0$ , the vortex strength  $\Gamma = 0.25$  and the Mach number  $M_s = 3$ .

In the Shock–Vortex interaction, an acoustic wavefront is generated and fine scale structures are formed behind the main shock. These are well captured by all three WENO schemes, with the same pattern as before, where less dissipation is noted at the WENO-Z and WENO-M solutions. The density  $\rho$  and velocity  $v$  at time  $t = 1$  computed by the WENO-Z scheme with grid resolution  $N_x = N_y = 400$  are shown in Fig. 11.

In Table 5, the CPU timing (in seconds) per Runge–Kutta step of the three WENO schemes for this problem shows that WENO-Z is the most efficient scheme and about 25% faster than the WENO-M scheme, since WENO-Z does not make use of any mapping to compute the weights.

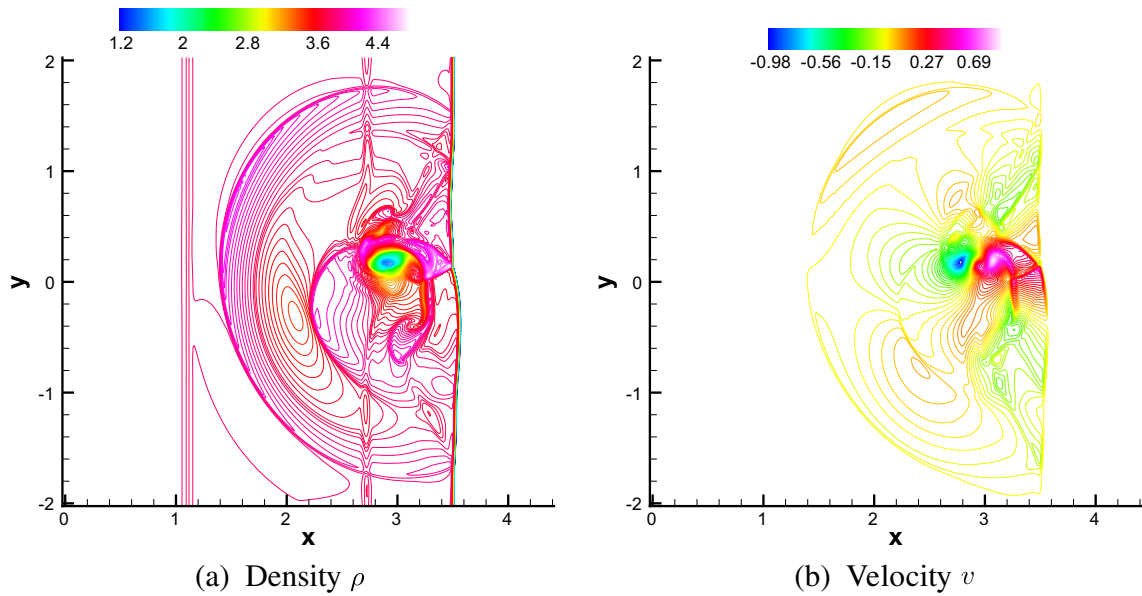


Fig. 11. (a) The density  $\rho$  and (b) the velocity  $v$  of the Mach 3 shock–vortex interaction at time  $t = 1$  and grid resolution  $N_x = N_y = 400$  as computed by the WENO-Z scheme.

Table 5

CPU timing (in seconds) per Runge–Kutta step of the shock–vortex interaction as computed by the WENO-JS, WENO-Z and WENO-M schemes

Grid size	WENO-JS	WENO-Z	WENO-M
$400 \times 400$	1.47	1.39	1.87
$800 \times 800$	6.54	6.15	8.27

### 5.3.2. Richtmyer–Meshkov instability

We use a rectangular domain  $[0, 5] \times [-1.8, 1.8]$  with a shock Mach number  $M_s = 4.46$  interacting with a single mode sinusoidal perturbed interface along a xenon (Xe) and argon (Ar) gases interface. The initial condition of the single mode Richtmyer–Meshkov instability is specified as follows:

- Rankine–Hugoniot conditions for the shock,
- Pre-shock temperature  $T = 296$  K,
- Pre-shock pressure  $P = 0.5$  atm,
- Xenon and Argon density are  $\rho_{Xe} = 2.90 \times 10^{-3} \frac{g}{cm^3}$  and  $\rho_{Ar} = 0.89 \times 10^{-3} \frac{g}{cm^3}$  respectively, at half of the normal atmospheric pressure,
- Specific heat ratio  $\gamma = \frac{5}{3}$ ,
- Atwood number  $At = 0.54$ ,
- Mach number  $M = 4.46$ ,
- Wave length  $\lambda = 3.6$  cm,
- Amplitude  $a = 1.0$  cm.
- The diffusive interface is modeled with an exponential function, i.e.

$$S(x, y) = \begin{cases} 1, & d \leq 0, \\ \exp(-\alpha|d|^\beta), & 0 < d < 1, \\ 0, & d \geq 1, \end{cases} \quad (57)$$

where

$$d = \frac{(x_s + a \cos(2\pi y/\lambda) + \delta) - x}{2\delta}, \quad (58)$$

$\delta = 0.2$  cm is the interface thickness,  $\beta = 8$  is the interface order,  $x_s = 0.5$  cm is the location of the interface and  $\alpha = -\ln \epsilon$ , where  $\epsilon$  is the machine zero. The conservative or primitive variables are scaled according to  $S(x, y)$  between the xenon and argon gases.

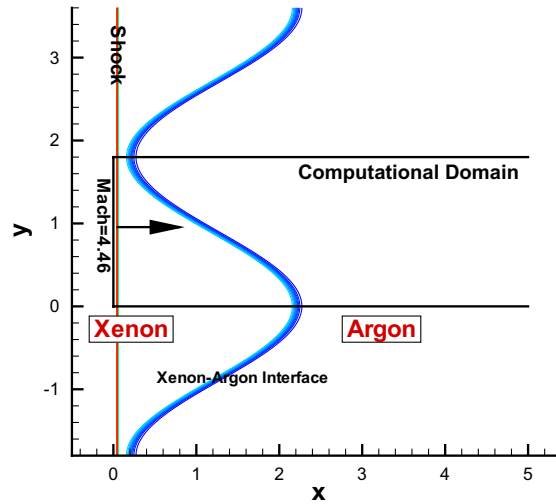


Fig. 12. The initial sinusoidal perturbation of the density  $\rho$  separating the xenon and argon gases at time  $t = 0$  for the Richtmyer–Meshkov Instability.

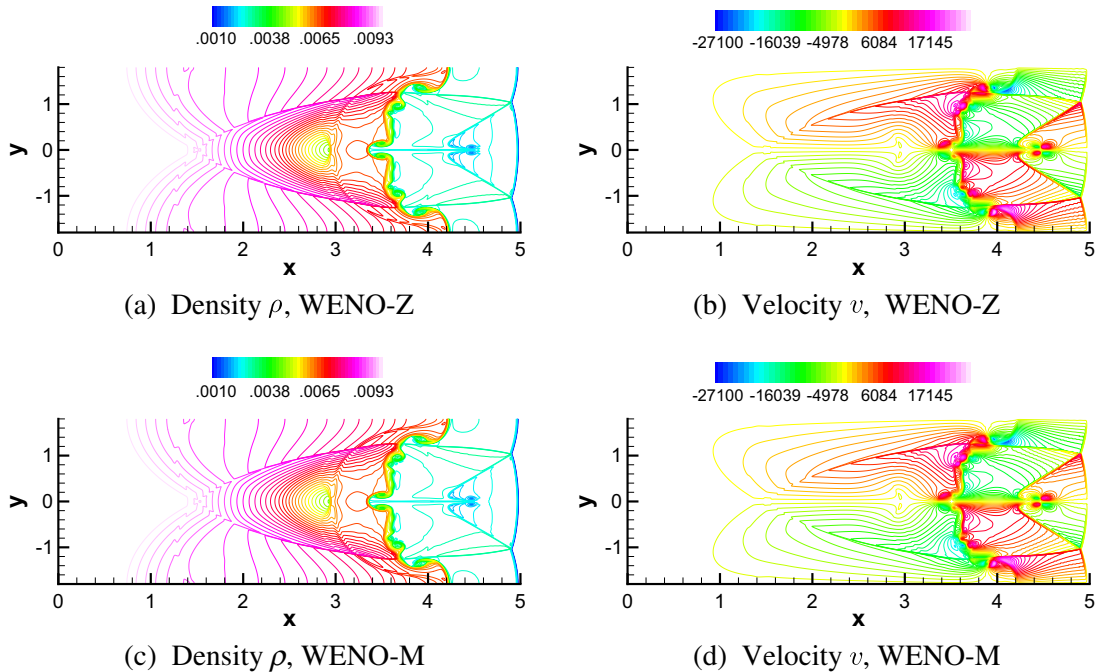


Fig. 13. Density,  $\rho$  and velocity,  $v$  of the Richtmyer–Meshkov Instability with Mach number  $M_s = 4.46$  at time  $t = 50 \mu s$  as computed by the (a–b) WENO-Z scheme and (c–d) WENO-M scheme with grid resolution  $N_x = N_y = 800$ .

Table 6

CPU timing (in seconds) per Runge–Kutta step of the Richtmyer–Meshkov instability problem as computed by the WENO-JS, WENO-Z and WENO-M schemes

Grid size	WENO-JS	WENO-Z	WENO-M
$800 \times 800$	6.46	6.07	8.13

The initial condition of the simulation is shown in Fig. 12. As the shock wave collides with the interface separating the two gases with different densities, the sinusoidal perturbed interface is accelerated, compressed and amplified following the transmission and refraction of the shock. Baroclinic vorticity generated along the gases interface amplifies the perturbation of the interface. The heavier xenon gas (Xe) will penetrate into the lighter argon gas (Ar) forming finger-like structures – bubbles and spikes. A bubble (spike) is a portion of the light (heavy) gas penetrating into the heavy (light) gas.

Fig. 13 shows the density  $\rho$  and velocity  $v$  at time  $t = 50 \mu\text{s}$  using the WENO-Z and WENO-M schemes with grid resolution  $N_x = N_y = 800$ . The results indicate that the WENO-Z scheme works very well for this class of problems, generating equivalent solutions as the WENO-M scheme.

Table 6 shows the CPU timing per Runge–Kutta step for all three WENO schemes at the grid resolution of  $N_x = N_y = 800$  with similar results as for the shock–vortex interaction.

## 6. Conclusions

We have devised an improved version of the fifth-order WENO finite differences scheme for conservation laws of [2] that makes use of higher order information already contained in the original framework of the classical WENO scheme. The new smoothness indicators proposed take into account the novel extra information on the regularity of the solution and provide a convex combination of stencils with enhanced order of convergence at critical points and less dissipation at shocks, but still non-oscillatory. The new WENO scheme generates numerical solutions with the same accuracy as the mapped WENO of [3] with smaller computational cost.

Our analysis also indicated that the improvements obtained by the mapped WENO over the classical scheme when solving problems with shocks are not due to its superior accuracy at critical points of the solutions, but to the larger weights it assigns to stencils with discontinuities. Similarly, the new WENO scheme assigns even larger weights to discontinuous stencils, obtaining solutions that are sometimes sharper, although its rate of convergence at critical points is intermediary between those schemes.

Research is currently underway to extend the new WENO idea to higher order WENO reconstruction schemes and will be reported at an upcoming paper

## Acknowledgements

The first, second and third authors have been supported by CNPq, Grant 300315/98-8. The fourth author gratefully acknowledges the support of this work by the DOE under Contract Number DE-FG02-98ER25346 and AFOSR under Contract Number FA9550-05-1-0123, and would also like to thanks the Departamento de Matemática Aplicada, IM-UFRJ, for hosting his visit during the course of the research.

## References

- [1] D. Balsara, C.W. Shu, Monotonicity preserving weighted essentially non-oscillatory schemes with increasingly high order of accuracy, J. Comput. Phys. 160 (2000) 405–452.
- [2] G.S. Jiang, C.W. Shu, Efficient implementation of weighted ENO schemes, J. Comput. Phys. 126 (1996) 202–228.
- [3] A.K. Henrick, T.D. Aslam, J.M. Powers, Mapped weighted essentially non-oscillatory schemes: achieving optimal order near critical points, J. Comput. Phys. 207 (2005) 542–567.
- [4] P.L. Roe, Approximation Riemann solvers, parameter vectors, and difference schemes, J. Comput. Phys. 43 (1981) 357.
- [5] C.W. Shu, S. Osher, Efficient implementation of essentially non-oscillatory shock-capturing schemes, J. Comput. Phys. 77 (1988) 439–471.

- [6] C.W. Shu, S. Osher, Efficient implementation of essentially non-oscillatory shock-capturing schemes, II, *J. Comput. Phys.* 83 (1) (1989) 32–78.
- [7] P. Woodward, P. Collela, The numerical simulation of two dimensional fluid flow with strong shocks, *J. Comput. Phys.* 54 (1984) 115–173.
- [8] D.A. Kopriva, Spectral collocation computation of the sound generated by a shock–vortex interaction, in: D. Lee, M.H. Schultz (Eds.), *Computational Acoustics: Algorithms and Applications*, vol. 2, 1988.